THz and sub-THz antiferromagnetic magnons via magnetoacoustic resonances excited by picosecond strain pulses in NiO

Andrei V. Azovtsev [*] and Nikolay A. Pertsev
Ioffe Institute, 194021 St. Petersburg, Russia

Antiferromagnets can host ultrafast spin dynamics in the terahertz (THz) frequency range, but an energy-efficient generation of THz magnons necessary for high-speed information processing devices is challenging. Fortunately, some antiferromagnetic compounds possess substantial magnetoelastic coupling between spins and strains, which opens the way for their excitation by mechanical stimuli. Here, we report a theoretical study of the spin dynamics excited in single-crystalline NiO by picosecond acoustic pulses, which can be created by optomechanical transducers driven by femtosecond laser pulses. To describe the interrelated spin and strain dynamics in this antiferromagnet distinguished by a strong magnetoelastic coupling, we carry out micromagnetoelastic simulations based on the numerical solution of the Landau-Lifshitz-Gilbert equation for sublattice magnetizations and the elastodynamic equation for mechanical displacements. The simulations show that the propagating "bipolar" pulse of the longitudinal strain generates correlated clockwise and counterclockwise precessions of the sublattice magnetizations, which have a complex spatial distribution in the region behind the pulse front. The spatiotemporal analysis of the simulation data reveals that the spin dynamics excited by the pulses with durations τ smaller than about 7 ps comprises a monochromatic spin wave with the frequency $\nu \approx 450$ GHz. Moreover, a second monochromatic spin wave having the frequency $\nu \approx 2$ THz emerges at $\tau \lesssim 3$ ps. By comparing the calculated dispersion of spin and elastic waves in NiO we demonstrate that the revealed monochromatic magnons originate from two magnetoacoustic resonances existing in this antiferromagnetic compound. Importantly, the acoustic pulses with durations $\tau \lesssim 3$ ps appear to be capable of creating antiferromagnetic magnons with THz and sub-THz frequencies in the absence of external magnetic fields. Our findings shed light on the magnetoacoustic phenomena in antiferromagnets and indicate that the single-crystalline NiO is a promising material for the development of ultrafast magnonic devices with a low power consumption.

I. INTRODUCTION

Antiferromagnets are considered as promising materials for spintronics because they are robust against the influence of magnetic fields, do not create stray fields, and demonstrate ultrafast spin dynamics in the terahertz frequency range [1–3]. However, the development of "antiferromagnetic spintronics" requires the elaboration of efficient methods for the excitation and control of spin dynamics in antiferromagnets and techniques enabling reliable detection of their magnetic states. Since the magnetic means of excitation suffer from several significant deficiencies (necessity to generate strong fields, high energy consumption, and scaling problems), it is of primary importance to study processes induced in antiferromagnets by nonmagnetic stimuli, such as electric currents and fields, optical pulses, and elastic strains. Previous theoretical and experimental studies in this field have been largely devoted to spin phenomena caused by electric currents [1,4,5]. Importantly, the electric currents flowing in heavy metals and topological insulators generate significant transverse spin currents, which exert a spin-orbit torque (SOT) on spin lattices in

ferromagnets and antiferromagnets brought into contact with such materials [6]. Therefore, current-induced reorientations of the Néel vector can be realized in nanostructures comprising ultrathin antiferromagnetic layers and nonmagnetic conductors with a strong spin-orbit coupling [1,4]. In particular, it is revealed experimentally that the antidamping SOT in NiO/Pt bilayers orients the Néel vector towards the direction of the writing electric current when its density exceeds $\sim 10^7$ A cm^{-2} [7]. Furthermore, in antiferromagnetic crystals where spin sublattices form space-inversion partners, the electric current flowing through the lattice can induce a relativistic spin torque, whose staggered fieldlike component can trigger ultrafast spin-axis reorientation [8]. The current-induced reorientations of the Néel vector observed in the CuMnAs and Mn$_2$Au films have been attributed to the action of such staggered spin-orbit fields [9–11]. Since the electrical readout of the spin reorientation can be realized via measurements of the linear-response anisotropic magnetoresistance [9] or second-order magnetotransport coefficient [11], it is possible to design an antiferromagnetic solid-state memory with both electrical writing and readout [9,11]. However, the density of the writing current should be well above 10^6 A cm^{-2} [9–11], which points to rather high Ohmic losses that accompany the functioning of such a memory.

*azovtsev@mail.ioffe.ru

Importantly, antiferromagnets exhibit the phenomenon of magnetostriction caused by the magnetoelastic coupling between spins and strains, and their magnetostrictive deformations can be comparable to those in ferromagnets [12–15]. Hence, antiferromagnetic compounds may have significant magnetoelastic coupling constants, which makes it possible to change magnetic states of antiferromagnetic materials by mechanical stimuli. This feature, which has been confirmed by recent experimental studies [16–25], provides an opportunity to realize an energy-efficient electrical control of antiferromagnets via their interfacial coupling to piezoelectric materials [26]. Indeed, the electrical switching of the Néel vector was realized in the antiferromagnetic Mn_2Au film grown on the ferroelectric PMN-PT substrate experiencing large piezoelectric deformations in applied electric fields [22]. Such a switching results from changes in the magnetic anisotropy caused by anisotropic in-plane film strains created by the substrate [22]. Significant strain-driven spin reorientations were also revealed in antiferromagnetic MnPt films grown on PMN-PT [23]. Owing to the phenomenon of anisotropic magnetoresistance, these reorientations manifest themselves in changes of the film conductivity and lead to the appearance of two nonvolatile resistance states switchable by the substrate piezoelectric strains but insensitive to strong magnetic fields [23].

The magnetoelastic effects in antiferromagnets have been studied theoretically since the middle of the 20th century [27,28]. The early theoretical studies were mostly focused on analytical calculations of magnetoelastic waves in bulk antiferromagnets [27,29,30]. Effects of external stresses on the antiferromagnetic resonance, magnetoelastic waves, and spin reorientation transitions were analyzed as well [29,31]. More recent theoretical research includes analytical studies of dynamic magnetoelastic phenomena in antiferromagnetic films and heterostructures [32–34] and first-principles calculations of the strain effects on magnetic states of FeRh [16,17] and various Mn-based antiferromagnets [35,36]. Besides, a numerical modeling of the strain-driven dynamics of antiferromagnetic moments has been performed recently [37]. Using finite-element calculations of the coupled magnetic and elastic dynamics, the authors modeled the strain-induced antiferromagnetic switching in a nanodisk bonded to a piezoelectric substrate [37], but the cross terms in the magnetoelastic energy that depend on the magnetizations of both sublattices were ignored in this study. The same approximation was used in the simulations of the acoustic excitation of magnons in the polycrystalline film of the easy-axis antiferromagnet $Fe_{50}Mn_{50}$ [38]. Overall, the behavior of antiferromagnets under mechanical stimuli remains to be largely unexplored and requires further theoretical investigations, especially the excitation of spin dynamics in antiferromagnets by injected elastic waves and short strain pulses created by piezoelectric and optical transducers.

In this paper, we report the results of numerical simulations of the interrelated spin and elastic dynamics generated by strain pulses in the single-crystalline NiO. Our advanced micromagnetoelastic modeling is distinguished from the preceding numerical studies by the correct description of the two-way magnetoelastic coupling between the Néel vector and lattice strains. The simulations are performed with the
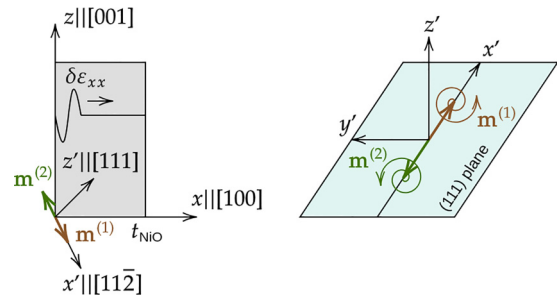

FIG. 1. Bipolar pulse $\delta\varepsilon_{xx}(x,t)$ of the longitudinal strain and strain-induced precession of sublattice magnetizations in the (100)-oriented NiO film with thickness t_{NiO}. The unit vectors $\mathbf{m}^{(1)}$ and $\mathbf{m}^{(2)}$ show the magnetizations' orientations relative to the crystallographic directions of the prototypic cubic phase of NiO. Two coordinate systems, (x, y, z) and (x', y', z'), are used in this study.

aid of an in-house software previously used to quantify the strain-induced magnetization dynamics in ferromagnetic films [39–41]. The upgraded version of this software makes it possible to describe magnetoelastic phenomena occurring in antiferromagnetic and ferrimagnetic crystals via the introduction of two spin sublattices. Since the inertial effects can modify the high-frequency spin dynamics [42–44], and they are expected to be especially important in the case of antiferromagnets [45,46], our model also allows for the influence of spin inertia on the generation of antiferromagnetic magnons. Nickel oxide is chosen for numerical calculations because this antiferromagnetic compound has a high Néel temperature $T_N = 523$ K and our analysis of the experimental data [47] shows that the single-crystalline NiO has very high magnetoelastic constants exceeding 10^8 erg cm^{-3}.

II. MICROMAGNETOELASTIC MODELING

The interrelated spin and acoustic dynamics in magnetoelastic materials can be modeled by solving a system of coupled differential equations comprising the Landau-Lifshitz-Gilbert (LLG) equation and the dynamical equation of the elasticity theory appended by magnetoelastic terms [48,49]. For antiferromagnets and ferrimagnets, it is necessary to introduce at least two spin sublattices and operate with their local magnetizations $\mathbf{M}^{(p)}(\mathbf{r}, t)$ ($p = 1, 2$). Since well below the Néel temperature the magnitudes $|\mathbf{M}^{(p)}| = M_s^{(p)}$ of sublattice magnetizations can be regarded as constant quantities at a given temperature, it is sufficient to consider the unit vectors $\mathbf{m}^{(p)} = \mathbf{M}^{(p)}/M_s^{(p)}$ defining the magnetization directions in the crystal lattice (Fig. 1). Taking into account that inertial effects may play a role at THz spin dynamics [42–44], we write the LLG equation for $\mathbf{m}^{(p)}$ as [46,50]

$$\frac{d\mathbf{m}^{(p)}}{dt} = -\gamma_p \mathbf{m}^{(p)} \times \mathbf{H}_{\text{eff}}^{(p)} + \alpha_p \mathbf{m}^{(p)} \times \frac{d\mathbf{m}^{(p)}}{dt}$$
$$+ \tau_p \mathbf{m}^{(p)} \times \frac{d^2\mathbf{m}^{(p)}}{dt^2}, \tag{1}$$

where $\mathbf{H}_{\text{eff}}^{(p)}$ is the effective magnetic field acting on the sublattice magnetization $\mathbf{M}^{(p)}$, while γ_p, α_p, and τ_p denote the electron's gyromagnetic ratio, dimensionless Gilbert damping

parameter, and angular momentum relaxation time, respectively, which are assumed to have the same values for both sublattices in this work. The effective field is the sum of the external magnetic field $\mathbf{H}$, field $\mathbf{H}_{dip}^{(p)}$ caused by dipolar interactions between spins, and contributions resulting from the intersublattice and intrasublattice exchange interactions, magnetocrystalline anisotropy, and magnetoelastic coupling between spins and strains. As spin rotations modify the strain state of a magnetoelastic material, the dynamical equation for the mechanical displacements $\mathbf{u}(\mathbf{r}, t)$ of material points contains additional magnetoelastic terms depending on the directions $\mathbf{m}^{(p)}(\mathbf{r}, t)$ of both sublattice magnetizations. Therefore, Eq. (1) should be solved together with the elastodynamic equation

$$\rho \frac{\partial^2 \mathbf{u}}{\partial t^2} = \nabla \boldsymbol{\sigma}, \qquad (2)$$

where ρ is the mass density and $\boldsymbol{\sigma}$ is the Cauchy stress tensor including the magnetoelastic term $\boldsymbol{\sigma}_{mel}$. In the simulations, the antiferromagnetic material is modeled by an ensemble of N nanoscale computational cells characterized by the spatial positions $\mathbf{r}_n$ of their centers and the vectors $\mathbf{m}^{(1)}(\mathbf{r}_n, t)$, $\mathbf{m}^{(2)}(\mathbf{r}_n, t)$, and $\mathbf{u}(\mathbf{r}_n, t)$ ($n = 1, 2, \ldots, N$).

The magnetoelastic contributions to the effective fields $\mathbf{H}_{eff}^{(p)}$ and the stress tensor components σ_{ij} ($i, j = x, y, z$) can be calculated by differentiating the magnetoelastic energy density F_{mel} with respect to the sublattice magnetizations $\mathbf{M}^{(p)}$ and strains ε_{ij}, respectively. In the case of antiferromagnets, the magnetoelastic energy density F_{mel} should be considered as the sum of the contributions depending on the components of the Néel vector $\mathbf{L} = (\mathbf{M}^{(1)} - \mathbf{M}^{(2)})/2$ and the mean magnetization $\mathbf{M} = (\mathbf{M}^{(1)} + \mathbf{M}^{(2)})/2$. However, in the ground ($\mathbf{M} = 0$) and weakly magnetized ($\mathbf{M} \ll \mathbf{L}$) states considered in this work, only the Néel vector contribution is essential [32]. Accordingly, the magnetoelastic energy density can be written in the first approximation as $F_{mel} = B_{ijkl} l_i l_j \varepsilon_{kl}$, where $\mathbf{l} = \mathbf{L}/M_s = (\mathbf{m}^{(1)} - \mathbf{m}^{(2)})/2$ and $M_s = M_s^{(1)} = M_s^{(2)}$ is the saturation magnetization of each sublattice. For antiferromagnets with the cubic paramagnetic phase, the energy density F_{mel} takes the form

$$\begin{aligned} F_{mel} = {} & B_1 \left(\varepsilon_{xx} l_x^2 + \varepsilon_{yy} l_y^2 + \varepsilon_{zz} l_z^2 \right) \\ & + B_2 [(\varepsilon_{xy} + \varepsilon_{yx}) l_x l_y + (\varepsilon_{xz} + \varepsilon_{zx}) l_x l_z + (\varepsilon_{yz} + \varepsilon_{zy}) l_y l_z] \end{aligned}$$
$$(3)$$

in the reference frame of this phase. Hence the magnetoelastic effective field $\mathbf{H}_{mel}^{(p)} = (-1/M_s) \partial F_{mel} / \partial \mathbf{m}^{(p)}$ is given by

$$H_x^{mel(p)} = (-1)^p \left[\frac{B_1}{M_s} \varepsilon_{xx} l_x + \frac{B_2}{M_s} (\varepsilon_{xy} l_y + \varepsilon_{xz} l_z) \right],$$

$$H_y^{mel(p)} = (-1)^p \left[\frac{B_1}{M_s} \varepsilon_{yy} l_y + \frac{B_2}{M_s} (\varepsilon_{yx} l_x + \varepsilon_{yz} l_z) \right],$$

$$H_z^{mel(p)} = (-1)^p \left[\frac{B_1}{M_s} \varepsilon_{zz} l_z + \frac{B_2}{M_s} (\varepsilon_{zx} l_x + \varepsilon_{zy} l_y) \right]. \qquad (4)$$

Since the magnetoelastic stress $\boldsymbol{\sigma}_{mel}$ is defined by the relations $\sigma_{ij}^{mel} = \partial F_{mel} / \partial \varepsilon_{ij}$, we obtain the total stresses σ_{ij}

as

$$\begin{aligned} \sigma_{xx} &= c_{11} \varepsilon_{xx} + c_{12}(\varepsilon_{yy} + \varepsilon_{zz}) + B_1 l_x^2, \\ \sigma_{yy} &= c_{11} \varepsilon_{yy} + c_{12}(\varepsilon_{xx} + \varepsilon_{zz}) + B_1 l_y^2, \\ \sigma_{zz} &= c_{11} \varepsilon_{zz} + c_{12}(\varepsilon_{yy} + \varepsilon_{xx}) + B_1 l_z^2, \\ \sigma_{xy} &= 2c_{44} \varepsilon_{xy} + B_2 l_x l_y, \\ \sigma_{xz} &= 2c_{44} \varepsilon_{xz} + B_2 l_x l_z, \\ \sigma_{yz} &= 2c_{44} \varepsilon_{yz} + B_2 l_y l_z, \end{aligned} \qquad (5)$$

where c_{11}, c_{12}, and c_{44} are the elastic stiffnesses of the prototypical cubic phase. Using the relations $l_i = (m_i^{(1)} - m_i^{(2)})/2$, one can rewrite Eqs. (4) and (5) in terms of the direction cosines of the sublattices' magnetizations $\mathbf{M}^{(p)}$. Importantly, this procedure shows that each of the magnetoelastic effective fields depends on both $m_i^{(1)}$ and $m_i^{(2)}$, which was not taken into account in the previous simulations of strain driven spin dynamics in antiferromagnets [37,38].

The total effective field $\mathbf{H}_{eff}^{(p)}$ also includes significant contribution resulting from the dipolar interactions between spins, which play an important role in NiO [28,51,52]. In particular, they determine the orientations of the easy planes, which appear to be parallel to the {111} crystallographic planes [51]. Since the rigorous calculation of the dipolar interactions between all individual spins requires the introduction of eight sublattices [52], we evaluate the dipolar fields in an approximation compatible with our two-sublattice model. Namely, total dipolar field is considered as the sum of the two contributions depending on the Néel vector $\mathbf{L}$ and the mean magnetization $\mathbf{M}$, respectively. The first contribution allows for the easy-plane anisotropy of dipolar origin, which is defined by the energy density $F_{anis}^{dip} = K_0' l_{z'}^2 = K_0 (l_x + l_y + l_z)^2$, where $l_{z'}$ is the projection of the normalized Néel vector $\mathbf{l}$ on the [111] crystallographic axis, and $K_0 = K_0'/3$. The second contribution represents the long-range magnetic field $\delta \mathbf{H}_{dip}(\mathbf{r}, t)$, which appears in the presence of nonzero mean magnetization $\mathbf{M}(\mathbf{r}, t)$ in the antiferromagnet and originates from its spatial inhomogeneity. The field $\delta \mathbf{H}_{dip}(\mathbf{r}, t)$ is calculated by summing the fields created by uniformly magnetized rectangular prisms with the magnetizations $\mathbf{M}(\mathbf{r}_n, t)$, which model the computational cells with the sizes smaller than the exchange length [53].

In addition to the easy-plane anisotropy of dipolar origin, a weak easy-axis anisotropy exists in NiO, which defines the energetically most favorable directions in the {111} crystallographic planes [28,54]. Since the easy axes are almost parallel to the $\langle 11\bar{2} \rangle$ directions [13], the corresponding energy density can be written as $F_{anis}^{ea} = K_1' l_{y'}^2 = K_1 (l_x - l_y)^2$, where $l_{y'}$ is the projection of the Néel vector on the direction in the (111) plane, which is orthogonal to the [11$\bar{2}$] one, and $K_1 = K_1'/2$. Hence the sum of the easy-plane and easy-axis anisotropies in the cubic reference frame has the form

$$F_{anis} = K_0 (l_x + l_y + l_z)^2 + K_1 (l_x - l_y)^2, \qquad (6)$$

and the total anisotropy contribution to the effective field $\mathbf{H}_{eff}^{(p)}$ can be calculated as $\mathbf{H}_{anis}^{(p)} = (-1/M_s) \partial F_{anis} / \partial \mathbf{m}^{(p)}$ by differentiating Eq. (6) rewritten in terms of the direction cosines $m_i^{(p)}$ of the sublattice magnetizations. Note that $\mathbf{H}_{anis}^{(p)}$ includes

the aforementioned first contribution to the dipolar field $\mathbf{H}_{\mathrm{dip}}^{(p)}$ so that $\mathbf{H}_{\mathrm{dip}}^{(p)}$ is set equal to $\delta\mathbf{H}_{\mathrm{dip}}^{(p)}(\mathbf{r}, t)$ in the numerical calculations.

To complete the description of the total effective fields $\mathbf{H}_{\mathrm{eff}}^{(p)}$ involved in Eq. (1), we have to specify the contributions of exchange interactions between the spins. In our model, the intersublattice interactions are quantified by an effective antiferromagnetic exchange, which keeps the sublattice magnetizations $\mathbf{m}^{(1)}(\mathbf{r}, t)$ and $\mathbf{m}^{(2)}(\mathbf{r}, t)$ antiparallel in the absence of perturbing magnetic fields and internal stresses. The corresponding fields $\mathbf{H}_{\mathrm{afm}}^{(p)}$ determined using the molecular field theory are given by the relations $\mathbf{H}_{\mathrm{afm}}^{(1)} = \lambda\mathbf{m}^{(2)}$ and $\mathbf{H}_{\mathrm{afm}}^{(2)} = \lambda\mathbf{m}^{(1)}$, where λ represents a phenomenological parameter. Finally, the contributions $\mathbf{H}_{\mathrm{fm}}^{(p)}$ of the intrasublattice interactions governed by the ferromagnetic exchange between the nearest neighbors are calculated as

$$\mathbf{H}_{\mathrm{fm}}^{(p)} = \frac{2A}{M_s}\left[\frac{\partial^2\mathbf{m}^{(p)}}{\partial x^2} + \frac{\partial^2\mathbf{m}^{(p)}}{\partial y^2} + \frac{\partial^2\mathbf{m}^{(p)}}{\partial z^2}\right]. \tag{7}$$

The phenomenological parameters λ and A are evaluated for NiO as described in Sec. III.

To carry out micromagnetoelastic simulations of the spin dynamics in NiO, we use homemade software, which numerically integrates Eq. (1) by the projective Runge-Kutta algorithm with a fixed integration step $\delta t = 20$ fs and solves Eq. (2) by a finite-difference technique with a midpoint derivative approximation [41]. Both techniques belong to the class of explicit finite-difference methods. The convergence of the integration of Eq. (2) in one dimension (1D) is ensured by fulfilling the condition $c < \delta x / \delta t$, where δx is the computational cell size and c is the highest elastic wave velocity present in the problem (in our case, c equals the velocity c_L of the longitudinal elastic waves in NiO). The convergence of the integration of the LLG equation has been tested numerically in separate preliminary simulations by picking small enough δt for given δx and magnetic parameters of the material. The considered (100)-oriented NiO film (Fig. 1) is modeled by an ensemble of cubic computational cells with the size $\delta x = 0.417$ nm equal to the lattice constant of NiO. The dynamical variables $\mathbf{m}^{(p)}(\mathbf{r}_n, t)$ and $\mathbf{u}(\mathbf{r}_n, t)$ are assumed to vary only along the x direction orthogonal to the film surfaces, and the calculation of the dipolar field $\delta\mathbf{H}_{\mathrm{dip}}(\mathbf{r}_n, t)$ is done using periodic boundary conditions imposed in the film plane [53]. Hence, we are solving a pseudo-1D problem corresponding to the NiO film with infinite in-plane dimensions, which is subjected to an external mechanical impact uniformly distributed along the in-plane y and z directions.

In the numerical calculations, we employ the material parameters of single-crystalline NiO. The phenomenological exchange parameters $\lambda = -5.8 \times 10^6$ Oe and $A = 1.59 \times 10^{-8}$ erg cm^{-1} and anisotropy constants $K_0' = 4.25 \times 10^6$ erg cm^{-3} and $K_1' = 1.8 \times 10^5$ erg cm^{-3} of NiO are evaluated as described in Sec. III. The elastic properties are defined by the stiffnesses $c_{11} = 3.3 \times 10^{12}$ erg cm^{-3}, $c_{12} = 0.6 \times 10^{12}$ erg cm^{-3}, and $c_{44} = 1.1 \times 10^{12}$ erg cm^{-3} of the paramagnetic NiO extrapolated to room temperature [55]. The set of material parameters also includes the electron's gyromagnetic ratio $\gamma_p = 1.919 \times 10^7$ G^{-1} s^{-1} corresponding

to the measured g-factor $g = 2.18$ [56], sublattice magnetization $M_s = 382$ emu cm^{-3} [57], Gilbert damping parameter $\alpha_p = 5 \times 10^{-4}$ [58], and mass density $\rho = 6.853$ g cm^{-3} [55]. Since the relaxation time τ_p is unknown for NiO, we first perform simulations without the account of the inertial term in Eq. (1) and then analyze its possible influence on the acoustic excitation of antiferrromagnetic magnons in NiO.

III. DETERMINATION OF MAGNETOELASTIC CONSTANTS AND EFFECTIVE EXCHANGE PARAMETERS OF NiO

The reliable determination of the magnetoelastic constants B_1 and B_2 of an antiferromagnetic single crystal requires the knowledge of its spontaneous strains and the orientation of the Néel vector. Fortunately, the spontaneous strains $\varepsilon_{i'j'}^0$ ($i', j' = x', y', z'$) of the single-crystalline NiO discussed in this paper have been measured by the x-ray diffraction topography [13,47]. The experimental data [47] show that $\varepsilon_{x'x'}^0 - \varepsilon_{y'y'}^0 \approx -9 \times 10^{-5}$ and $\varepsilon_{x'z'}^0 + \varepsilon_{z'x'}^0 \approx 1.6 \times 10^{-5}$ in the rotated reference frame with the axes x', y', z' parallel to the $[11\bar{2}]$, $[\bar{1}10]$, and $[111]$ crystallographic directions, respectively [59]. Taking into account that the Néel vector is almost parallel to the $[11\bar{2}]$ direction [13,47] and setting the stresses σ_{ij} in Eq. (5) to zero, we obtain the following relations for the spontaneous strains in the rotated reference frame:

$$\varepsilon_{x'x'}^0 = \frac{-B_1 c_{11}}{2(c_{11} - c_{12})(c_{11} + 2c_{12})} - \frac{B_2}{4c_{44}},$$

$$\varepsilon_{y'y'}^0 = \frac{B_1}{6}\left(\frac{1}{c_{11} - c_{12}} - \frac{2}{c_{11} + 2c_{12}}\right) + \frac{B_2}{12c_{44}},$$

$$\varepsilon_{z'z'}^0 = \frac{1}{6}\left(\frac{-2B_1}{c_{11} + 2c_{12}} + \frac{B_2}{c_{44}}\right),$$

$$\varepsilon_{x'z'}^0 = \varepsilon_{z'x'}^0 = \frac{1}{6\sqrt{2}}\left(\frac{2B_1}{c_{11} - c_{12}} - \frac{B_2}{c_{44}}\right),$$

$$\varepsilon_{x'y'}^0 = \varepsilon_{y'x'}^0 = \varepsilon_{y'z'}^0 = \varepsilon_{z'y'}^0 = 0, \tag{8}$$

where the material constants are defined in the crystallographic frame (x, y, z). The formulas for the difference $\varepsilon_{x'x'}^0 - \varepsilon_{y'y'}^0$ and the shear strain $\varepsilon_{x'z'}^0$ give the system of equations enabling us to evaluate the magnetoelastic constants B_1 and B_2. The calculation yields

$$B_1 = -(c_{11} - c_{12})\left(\varepsilon_{x'x'}^0 - \varepsilon_{y'y'}^0 - 2\sqrt{2}\varepsilon_{x'z'}^0\right),$$

$$B_2 = -2c_{44}\left(\varepsilon_{x'x'}^0 - \varepsilon_{y'y'}^0 + \sqrt{2}\varepsilon_{x'z'}^0\right). \tag{9}$$

Since the relevant elastic constants c_{ij} of the paramagnetic NiO are known [55], the magnetoelastic constants appear to be $B_1 \approx 3 \times 10^8$ erg cm^{-3} and $B_2 \approx 1.7 \times 10^8$ erg cm^{-3}. Substituting these values into Eq. (8), we find the rest of the spontaneous strains in the rotated reference frame as $\varepsilon_{x'x'}^0 \approx -8.1 \times 10^{-5}$, $\varepsilon_{y'y'}^0 \approx 9.4 \times 10^{-6}$, and $\varepsilon_{z'z'}^0 \approx 3.7 \times 10^{-6}$. As may be expected, the strain $\varepsilon_{x'x'}^0$ along the spin axis is much larger than the strains in the transverse directions. In the crystallographic reference frame (x, y, z), the spontaneous strains of the NiO single crystal with the $[11\bar{2}]$ orientation of the Néel vector are predicted to be $\varepsilon_{xx}^0 = \varepsilon_{yy}^0 \approx -3.7 \times 10^{-6}$, $\varepsilon_{zz}^0 \approx -6 \times 10^{-5}$, $\varepsilon_{xy}^0 \approx -1.3 \times 10^{-5}$, and $\varepsilon_{xz}^0 = \varepsilon_{yz}^0 \approx 2.6 \times 10^{-5}$.

Since the evaluated magnetoelastic constants B_1 and B_2 of the single-crystalline NiO are very high, the orientation of the Néel vector in this antiferromagnetic compound should be very sensitive to strains. This conclusion agrees with the experimental data on the Néel-vector direction in the epitaxial NiO films grown on (001)-oriented MgO [60]. Indeed, the measurements show that in such (001)-oriented films the Néel vector is oriented along the $[55\overline{19}]$ direction significantly differing from its $[11\overline{2}]$ orientation in the bulk NiO, which is attributed to the influence of substrate-induced strains [60]. Substituting the measured in-plane strains $\varepsilon_{xx} = \varepsilon_{yy} \approx 8.6 \times 10^{-3}$ in the epitaxial NiO film into Eq. (3), we determine the magnetoelastic energy F_{mel} as a function of the Néel-vector direction cosines l_i. The minimization of the sum of F_{mel}, elastic energy, and the energy of magnetocrystalline anisotropy F_{anis} given by Eq. (6) then shows that the energetically most favorable direction in the strained NiO films should be close to $[55\overline{19}]$ at the values of the magnetoelastic constants and anisotropy coefficients used in this paper. Namely, the calculated angle θ between the Néel-vector direction and the $[00\overline{1}]$ axis is about $22°$, whereas the measurements give $\theta = 20°$. Given the uncertainty in the angle θ and the in-plane strains in the MgO/NiO/Pt structure [60], the agreement with the experimental data should be regarded as excellent.

Now we turn to the evaluation of the effective exchange parameters λ and A and anisotropy constants K_0' and K_1' involved in our two-sublattice model of NiO. Appropriate values of λ, A, K_0', and K_1' can be found by reproducing the measured frequencies of two antiferromagnetic resonance (AFMR) modes [54,61,62] and the spin-wave dispersion determined by inelastic neutron scattering techniques [54]. To this end, we model the spin dynamics in the (100)-oriented NiO film with fixed in-plane strains ε_{yy}, ε_{zz}, and ε_{yz} set equal to the spontaneous strains given above. First, the relaxation of deflected spins to the equilibrium $[11\overline{2}]$ orientation is investigated at different values of λ, K_0', and K_1', which enables us to quantify the spin precession occurring during this process. The determined frequency of the precession out of the (111) easy plane is compared with the measured frequency $\nu_{\text{AFMR}}^{\text{high}} = 1100$ GHz of the higher AFMR mode [61,62], while the frequency of the in-plane precession is collated to the frequency $\nu_{\text{AFMR}}^{\text{low}} = 240$ GHz of the lower AFMR mode [54]. Second, we consider monochromatic spin waves excited at the NiO surface $x = 0$ by a fictitious local magnetic field $\mathbf{H}(x = 0, t)$ oscillating with a frequency ν and model their propagation across the NiO film at different values of the ferromagnetic exchange parameter A. The variation of the wave number k with the excitation frequency ν is then compared with the measured spin-wave dispersion [54]. By performing a series of simulations, we find that the agreement between theoretical and experimental results is attained at $\lambda = -5.8 \times 10^6$ Oe, $A = 1.59 \times 10^{-8}$ erg cm^{-1}, $K_0' = 4.25 \times 10^6$ erg cm^{-3}, and $K_1' = 1.8 \times 10^5$ erg cm^{-3}.

IV. SPIN DYNAMICS EXCITED IN NiO BY STRAIN PULSES

Micromagnetoelastic simulations are carried out for NiO films not subjected to magnetic fields ($\mathbf{H} = 0$) and epitaxial strains $[\varepsilon_{ij}(\mathbf{r}, t = 0) = \varepsilon_{ij}^0]$. The initial state of such films is
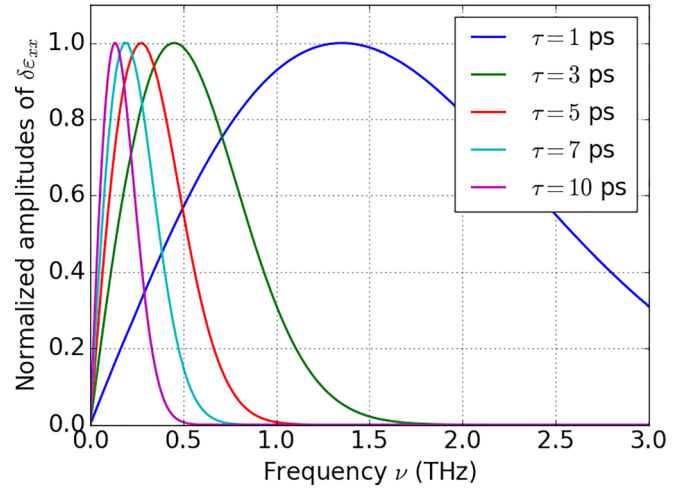

FIG. 2. Frequency spectra of strain pulses with different durations τ generated in NiO. The spectra show the normalized amplitudes of the Fourier transforms of the time dependences $\delta\varepsilon_{xx}(x, t)$ at the NiO surface $x = 0$. The pulse durations are indicated on the plot.

determined in the macrospin approximation by numerically finding the energetically most favorable spin orientation in the stress-free Ni crystal. The calculations show that the predicted initial spin orientation is very close to the $[11\overline{2}]$ direction, and the lattice strains only slightly differ from the spontaneous strains ε_{ij}^0 given in Sec. III. To generate a strain pulse $\delta\varepsilon_{xx}(x, t)$ in the NiO film, we introduce a time-dependent uniform displacement $\delta u_x(x = 0, t) = u_{\max} \exp(-t^2/\tau_u^2)$ at the film surface $x = 0$. Such a variable displacement should give rise to a "bipolar" strain pulse (Fig. 1) involving periods of compression and tension [41]. The parameters $u_{\max}$ and τ_u are tailored so as to produce the initial strain amplitude of 2×10^{-4} and a realistic pulse duration of a few picoseconds [63,64]. At the same time, the in-plane strains ε_{yy}, ε_{zz}, and ε_{yz} are kept equal to their initial values ε_{yy}^0, ε_{zz}^0, and ε_{yz}^0 throughout the film so that changes δu_y and δu_z in the in-plane displacements depend on the coordinate x only. The dynamics of the sublattice magnetizations $\mathbf{m}^{(p)}(x, t)$ and the lattice strains $\varepsilon_{xj}(x, t)$ are determined by numerically solving Eqs. (1) and (2) as described in Sec. II. The results presented in Figs. 3–5 below do not allow for the possible influence of the spin inertia, which is discussed later in the end of this section.

The simulations performed for the NiO film with the thickness $t_{\text{NiO}} = 834$ nm (2000 lattice constants) demonstrate the generation of a bipolar strain pulse near the surface, which propagates across the film and induces correlated counterclockwise and clockwise precessions of the sublattice magnetizations $\mathbf{m}^{(1)}$ and $\mathbf{m}^{(2)}$ around the $[11\overline{2}]$ easy axis (Fig. 1). Figure 2 shows representative frequency spectra of strain pulses with durations τ ranging from 1 to 10 ps. Remarkably, the spectra obtained at $\tau \leqslant 3$ ps contain significant components in the THz frequency range, which indicates the possibility of exciting THz antiferromagnetic magnons by picosecond acoustic pulses. As can be seen from Fig. 3, the spin dynamics generated by the propagating strain pulse has a complex spatial distribution, which involves the region of largest oscillations of the direction cosines $m_i^{(p)}(x, t)$ just
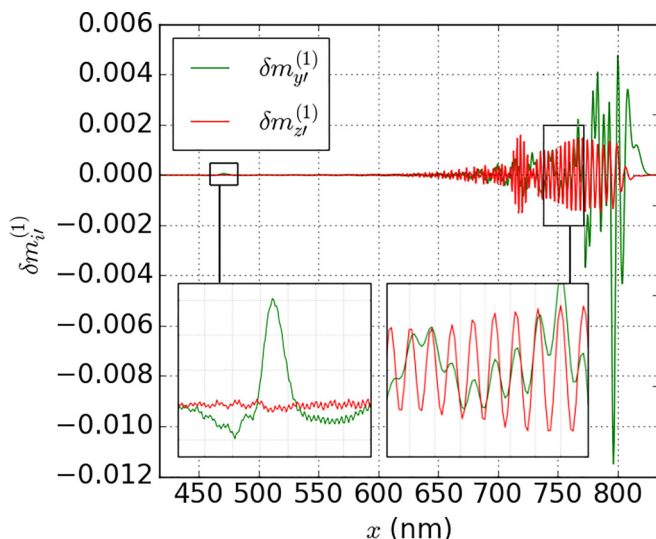
FIG. 3. Spatial distribution of the spin dynamics excited in NiO by a 1-ps-long strain pulse. The plots show changes $\delta m_{i'}^{(1)}(x,t)$ of the magnetization direction cosines in the first sublattice at the moment $t = 0.12$ ns. The insets show enlarged views of the intermediate region containing a THz monochromatic spin wave (right inset) and a peak of magnetization oscillations generated by a small pulse of shear strains created by the spin precessions induced by the primary pulse of the longitudinal strain (left inset).

after the pulse front followed by nonmonotonic variation of the oscillations' amplitude down to much smaller values far behind the front. Interestingly, there exists a small peak of the precession amplitudes, which gradually lags from the strain pulse moving with the velocity $c_L = \sqrt{c_{11}/\rho}$ of the longitudinal elastic wave (see the left inset in Fig. 3). The simulation data shows that the distance between this peak and the front increases with time as $(c_L - c_T)/t$, where $c_T = \sqrt{c_{44}/\rho}$ is the velocity of the transverse elastic wave in NiO. Therefore, we can attribute the revealed feature of the spin dynamics to its additional excitation by a pulse of transverse elastic strains $\varepsilon_{xy}(x,t)$ and $\varepsilon_{xz}(x,t)$. Such a *secondary* strain pulse is created by the precession of the sublattice magnetizations induced by the *primary* acoustic pulse $\delta\varepsilon_{xx}(x,t)$. This phenomenon is caused by the back action of the magnetization precession on lattice strains, and is similar to the generation of elastic waves by spin waves in ferromagnets [39,40,65].

Remarkably, the spatial distributions of the spin oscillations excited by the pulses with the durations $\tau \lesssim 7$ ps involve an intermediate region, where they have the form of *monochromatic* spin waves (see the right inset in Fig. 3). To determine the characteristics of such waves, we calculated the Fourier transforms of the magnetization oscillations $\delta m_{i'}^{(p)}(x,t)$ in the appropriate spatial and temporal intervals and plotted their amplitudes as functions of the frequency ν and the wave number k. Representative spectra shown in Fig. 4 demonstrate the presence of two peaks at the frequencies of about 450 GHz and 2 THz in the spectra obtained at the pulse durations of 1 and 3 ps. These peaks, which are absent at $\tau = 10$ ps, are characterized by the wave numbers

$k \approx 40 \times 10^5$ rad cm^{-1} and $k \approx 190 \times 10^5$ rad cm^{-1}, respectively. In should be noted that the ratio of the peak heights strongly depends on the pulse duration.

To clarify the origin of the revealed monochromatic spin waves, we compare the dispersion of antiferromagnetic magnons with the dispersion relation $\nu_L = c_L k/(2\pi)$ of the longitudinal elastic waves. For two-sublattice antiferromagnets, the dispersion relation can be written as [66]

$$\nu_{AFM}(k) = \sqrt{\nu_0^2 + [c_{AFM}k/(2\pi)]^2}, \qquad (10)$$

where ν_0 denotes the frequency of the lower or higher AFMR mode, and c_{AFM} is the velocity of the antiferromagnetic spin wave. The frequencies $\nu_{AFMR}^{low} = 240$ GHz and $\nu_{AFMR}^{high} = 1100$ GHz of these modes are known (see Sec. III), and $c_{AFM} = 5.9 \times 10^5$ cm s^{-1} is evaluated by fitting Eq. (10) to our simulation data on the propagation of monochromatic spin waves in NiO discussed in Sec. III. Figure 5 shows that the calculated dependences $\nu_{AFM}(k)$ and $\nu_L(k)$ cross at the wave numbers $k_{cross}^{low} \approx 40 \times 10^5$ rad cm^{-1} and $k_{cross}^{high} \approx 190 \times 10^5$ rad cm^{-1} yielding the crossing-point frequencies $\nu_{cross}^{low} \approx 450$ GHz and $\nu_{cross}^{high} \approx 2$ THz. Since the parameters of the crossing points are close to the frequencies and wave numbers of the monochromatic spin waves generated by the 1- and 3-ps-long acoustic pulses, we arrive at the conclusion that the excitation of such waves is due to the phenomenon of magnetoacoustic resonance [48,49]. Accordingly, the pulse spectrum should contain significant components at frequencies around ν_{cross}^{low} or ν_{cross}^{high} to be capable of generating monochromatic spin waves with considerable magnitudes.

Finally, we consider the possible influence of the spin inertia on the acoustic excitation of antiferromagnetic magnons in NiO. As the relaxation time τ_p involved in Eq. (1) is unknown for NiO, the range of its acceptable values is evaluated by analyzing the inertial corrections to the frequency ν_{AFMR}^{high} of the higher AFMR mode. To that end, we use the analytical relation $\nu_{AFMR}^{high} = [\gamma_p/(2\pi)]\sqrt{2K_0'|\lambda|/M_s}/\sqrt{1 + 2\tau_p\gamma_p|\lambda|}$ [45] and the constraint that the frequency ν_{AFMR}^{high} calculated with the account of the inertial effects and the $\pm 10\%$ error in the determined anisotropy constant $K_0' = 4.25 \times 10^6$ erg cm^{-3} should remain equal to the measured value of 1100 GHz [61,62]. This procedure yields the relaxation time τ_p ranging from about 0.5 to -0.5 fs, which looks reasonable in view of the numbers reported for ferromagnets [42], since τ_p can also take negative values in our notation [67].

To clarify the influence of the spin inertia on the magnetoacoustic resonances in NiO, we first derive the dispersion relation $\nu_{AFM}(k)$ of the antiferromagnetic magnons with the account of the inertial effects. This relation can be determined by linearizing the system of two LLG equations written for the sublattice magnetizations $\mathbf{m}^{(p)}$ slightly deviating from their equilibrium directions. Leaving out the magnetoelastic contribution to the effective fields $\mathbf{H}_{eff}^{(p)}$ and the magnetic damping in Eq. (1) and using the ansatz of plane spin waves, we obtain the secular equation ensuring the existence of a nontrivial solution of the considered system of equations. The solution of the
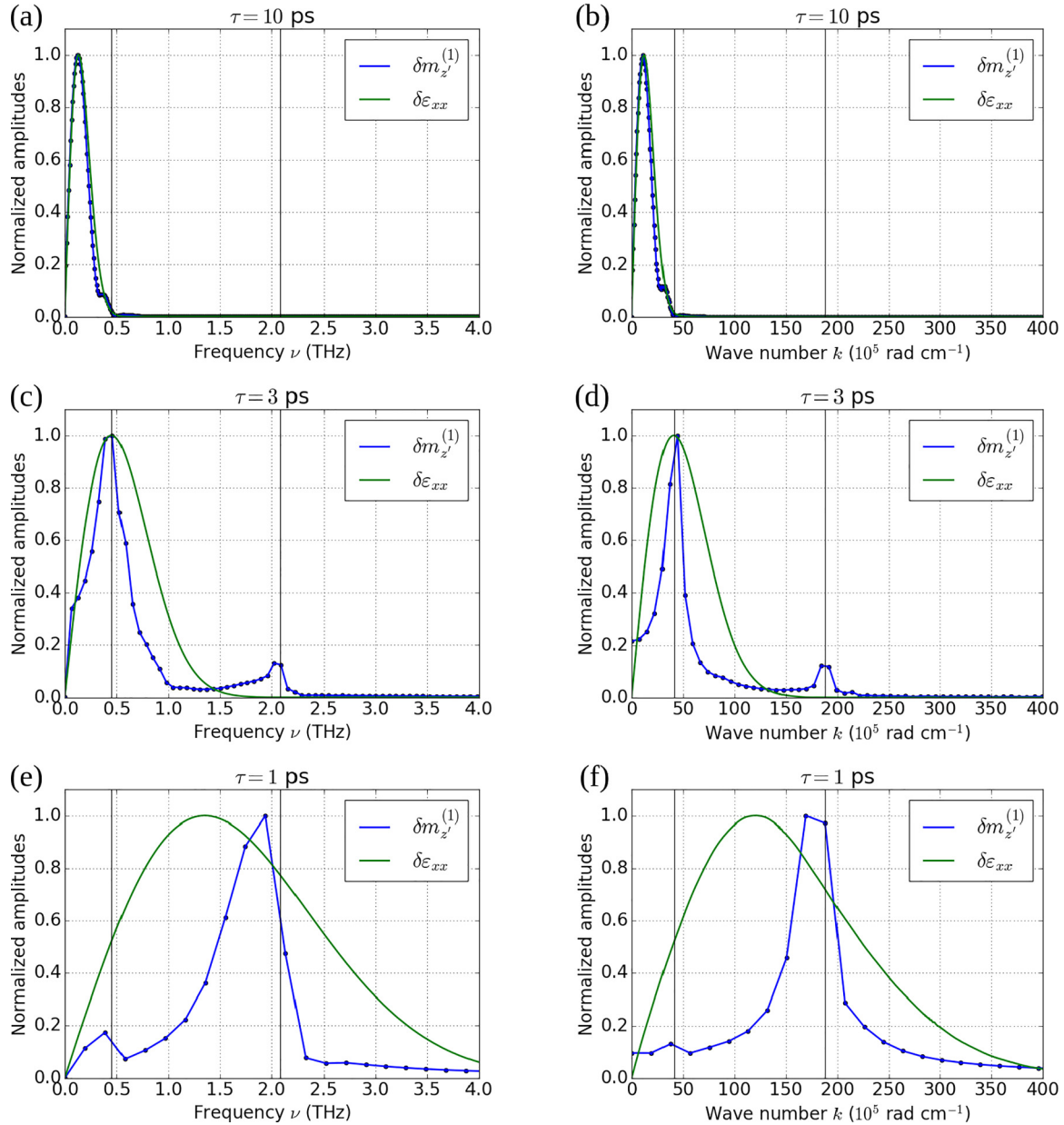
FIG. 4. Frequency and wave number spectra of magnetization dynamics excited by strain pulses with different durations in the selected intervals of the strain-induced spin oscillations. The plots show the temporal (a), (c), (e) and spatial (b), (d), (f) Fourier transforms of the magnetization oscillations $\delta m_{z'}^{(1)}(x, t)$. Frequency spectra are based on the time signal taken at $x = t_{\mathrm{NiO}}/2 = 417$ nm. The pulse front crosses this position at $t = 0.0595$ ns. The graphs are plotted for the following intervals: (a) [0, 0.12] ns, (c) [0.0647, 0.08] ns, (e) [0.0627, 0.0679] ns. Wave number spectra are based on the spatial profile of magnetization at $t = 0.12$ ns. The pulse front has the coordinate $x = 834$ nm, and the following spatial intervals on the x axis are used: (b) [0, 834] nm, (d) [730, 771] nm, (f) [738, 771] nm. Vertical lines denote the crossing-point frequencies and wave numbers discussed in the text. The pulse durations are indicated on the plots.

secular equation gives

$$\nu_{\mathrm{AFM}}(k) = \frac{1}{2\pi} \sqrt{\frac{1 + 2\beta + \tau_p \gamma_p \frac{K}{M_s} + 2\tau_p D k^2 \mp \sqrt{1 + 4\beta + 4\beta^2 + 2(1 - 2\beta)\tau_p \gamma_p \frac{K}{M_s} + 4\tau_p D k^2}}{2\tau_p^2}}, \tag{11}$$

where K denotes the anisotropy constant K_0' or K_1' yielding the higher or lower branch of the antiferromagnetic spin-wave dispersion, respectively, $\beta = \tau_p \gamma_p |\lambda|$ is the dimensionless parameter characterizing the relative strength of inertial effects

in a specific antiferromagnet, and $D = 2A\gamma_p/M_s$ is the spin wave stiffness. The minus sign before the nested square root in Eq. (11) provides the dispersion relation for the correlated precession of the sublattice magnetizations, while the plus sign
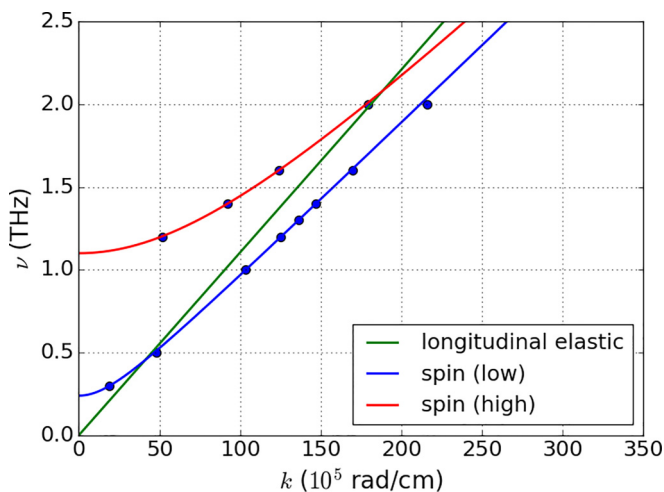
FIG. 5. Dispersion relations of spin and elastic waves in NiO. Points denote the results of micromagnetic simulations obtained for spin waves excited at the NiO surface $x = 0$ by a fictitious local magnetic field $\mathbf{H}(x = 0, t)$ oscillating with a frequency ν. The curves represent two branches of the spin-wave dispersion relation resulting from the fitting of Eq. (10) to the simulation data, while the straight line shows the dispersion of the longitudinal elastic waves in NiO.

corresponds to their coupled nutation. In the limit of $\tau_p \to 0$, Eq. (11) reduces to Eq. (10) with $c_{\mathrm{AFM}} = 2\gamma_p\sqrt{|\lambda|A/M_s}$ and $\nu_0 = [\gamma_p/(2\pi)]\sqrt{2K|\lambda|/M_s}$ at the minus sign and predicts an infinite nutation frequency at the plus sign. The good accuracy of the dispersion relation derived for the precession mode is supported by the agreement of Eq. (11) with the results of micromagnetic simulations performed with the account of inertial effects for antiferromagnetic magnons generated at the NiO surface by the fictitious local magnetic field.

Equation (11) predicts that the introduction of the nonzero relaxation time τ_p shifts the dispersion curves of the precession mode to lower frequencies at $\tau_p > 0$ and to higher frequencies at $\tau_p < 0$. The numerical results obtained for NiO at $\tau_p = 0.5$ fs and $\tau_p = -0.5$ fs are presented in Fig. 6. As the frequency $\nu_{\mathrm{AFMR}}^{\mathrm{high}}$ of the higher AFMR mode is kept fixed at the measured value of 1100 GHz, significant changes of the higher branch of $\nu_{\mathrm{AFM}}(k)$ appear only at the wave numbers k exceeding about 200×10^5 rad cm^{-1}. The lower branch demonstrates similar modifications, with the AFMR frequency $\nu_{\mathrm{AFMR}}^{\mathrm{low}}$ being almost unaffected by the spin inertia. Nevertheless, the crossing points of $\nu_{\mathrm{AFM}}(k)$ with the dispersion of longitudinal elastic waves experience notable shifts at the chosen values of the relaxation time τ_p. Namely, at $\tau_p = 0.5$ fs, the crossing-point frequencies $\nu_{\mathrm{cross}}^{\mathrm{high}}$ and $\nu_{\mathrm{cross}}^{\mathrm{low}}$ decrease from 2 THz to approximately 1.9 THz and from 450 GHz to about 370 GHz, respectively. In contrast, the calculation yields $\nu_{\mathrm{cross}}^{\mathrm{high}} \approx 2.7$ THz and $\nu_{\mathrm{cross}}^{\mathrm{low}} \approx 580$ GHz when $\tau_p = -0.5$ fs.

In order to validate the crossing-point frequencies and wave numbers predicted with the aid of Eq. (11), we run additional micromagnetoelastic simulations of the spin dynamics generated by the 1-ps-long acoustic pulse in the presence of inertial effects characterized by the relaxation times $\tau_p = \pm 0.5$ fs. In these simulations, a different integration scheme
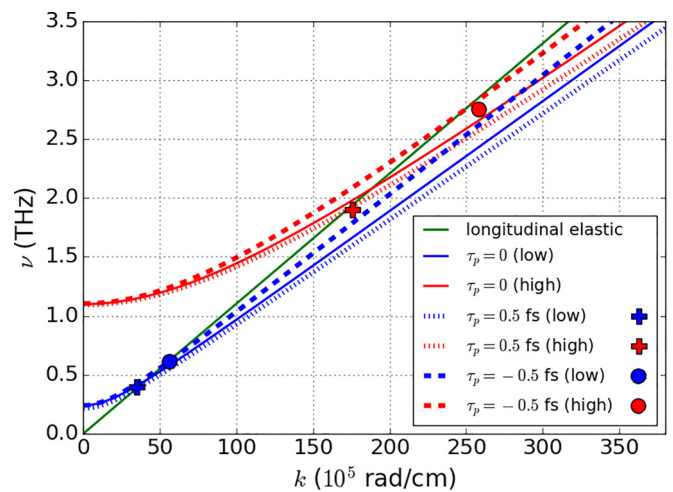

FIG. 6. Influence of spin inertia on the magnon dispersion and magnetoacoustic resonances in NiO. The curved dotted and dashed lines show the magnon dispersion relations calculated using Eq. (11) with the relaxation time τ_p equal to 0.5 fs and -0.5 fs, respectively. The cross and circle symbols denote the results of micromagnetoelastic simulations obtained for the frequencies and wave numbers of monochromatic spin waves generated by the 1-ps-long strain pulse. The straight green line indicates the dispersion of the longitudinal elastic waves in NiO, and the solid blue and red curves display the dispersion of antiferromagnetic magnons in the absence of inertial effects.

of the LLG equation is employed, which is a variant of the explicit projective Euler scheme adapted for the integration of Eq. (1) involving the inertial term. Since this scheme is a first-order algorithm unlike the previously used fourth-order Runge-Kutta method, the convergence is achieved by decreasing the integration time step down to $\delta t = 0.2$ fs. The simulations reveal the emerging nutation of sublattice magnetizations and quantitative changes in their precessional dynamics. Namely, the frequencies and wave numbers of the generated monochromatic spin waves shift towards higher or lower values depending on the sign of τ_p (see the cross and circle symbols in Fig. 6). Importantly, the parameters of these waves extracted from the simulation data show a good agreement with the crossing-point frequencies and wave numbers predicted by the analytical calculations. Therefore, the spin inertia should not prevent the generation of THz antiferromagnetic magnons in NiO subjected to picosecond acoustic pulses with sufficiently small durations.

V. CONCLUSION

In this paper, we theoretically studied the spin dynamics and magnetoelastic effects induced in the single-crystalline NiO by picosecond acoustic pulses. To quantify the energy density of NiO, we introduced a two-sublattice model, which employs effective intersublattice and intrasublattice exchange interactions and properly describes the magnetocrystalline and magnetoelastic anisotropies as functions of the Néel-vector components. The involved parameters of exchange interactions and magnetocrystalline anisotropies were evaluated by fitting the experimental data on the spin dynamics

in NiO [54,61,62], while the magnetoelastic constants were determined by reproducing the measured spontaneous strains of the NiO single crystal [47]. By adjusting our homemade software [39–41] to the two-sublattice model, we carried out micromagnetoelastic simulations of the coupled dynamics of sublattice magnetizations and lattice strains in the (100)-oriented NiO film subjected to the "bipolar" acoustic pulses with durations ranging from 1 to 10 ps.

The simulations show that the strain-induced spin dynamics has the form of correlated precessions of the sublattice magnetizations depicted in Fig. 1. The precessions' amplitudes reach maximal values near the pulse front and decrease nonmonotonically down to much smaller values far behind the front (Fig. 3). The frequency spectrum of the magnetization oscillations strongly depends on the pulse duration τ, being very similar to the smooth pulse spectrum at $\tau = 10$ ps but having pronounced features at $\tau \leqslant 7$ ps. Namely, the spatiotemporal analysis of the simulation data reveals that the spin dynamics induced by the pulses with $\tau \leqslant 7$ ps comprises a monochromatic spin wave with the frequency $\nu \approx 450$ GHz and the wave number $k \approx 40 \times 10^5$ rad cm^{-1}. Moreover, a second monochromatic spin wave with $\nu \approx 2$ THz and $k \approx 180 \times 10^5$ rad cm^{-1} emerges at $\tau \leqslant 3$ ps. Since the characteristics of such waves are close to the crossing points of the dispersion relations $\nu_{\mathrm{AFM}}(k)$ and $\nu_{\mathrm{L}}(k)$ shown in Fig. 5, their generation is attributed to the phenomenon of magnetoacoustic resonance, which occurs when spin and elastic waves have similar frequencies and wavelengths. As the generated monochromatic magnons modify the spectrum of elastic excitations, they could be regarded as antiferromagnetic magnetoelastic waves propagating in the NiO crystal. The magnetoelastic coupling between spins and strains also manifests itself in the revealed generation of a small pulse of *shear* strains ε_{xy} and ε_{xz}, which is created by the precession of the sublattice magnetizations induced by the primary pulse of the *longitudinal* strain.

Our theoretical results demonstrate that picosecond acoustic pulses propagating in the single-crystalline NiO can generate antiferromagnetic magnons with THz and sub-THz frequencies in the absence of external magnetic fields. Since such acoustic pulses can be created with the aid of femtosecond laser pulses [63], an efficient strain-driven generation of high-frequency magnons in antiferromagnets by optomechanical transducers is envisioned. Owing to the presence of magnetoacoustic resonances at sub-THz and THz frequencies and high magnetoelastic constants, NiO should be regarded as a promising material for the development of high-speed information processing devices.

[1] T. Jungwirth, X. Marti, P. Wadley, and J. Wunderlich, Nat. Nanotechnol. **11**, 231 (2016).

[2] V. Baltz, A. Manchon, M. Tsoi, T. Moriyama, T. Ono, and Y. Tserkovnyak, Rev. Mod. Phys. **90**, 015005 (2018).

[3] J. Han, R. Cheng, L. Liu, H. Ohno, and S. Fukami, Nat. Mater. **22**, 684 (2023).

[4] O. J. Amin, K. W. Edmonds, and P. Wadley, Appl. Phys. Lett. **117**, 010501 (2020).

[5] A. R. Safin, S. A. Nikitov, A. I. Kirilyuk, D. V. Kalyabin, A. V. Sadovnikov, P. A. Stremoukhov, M. V. Logunov, and P. A. Popov, J. Exp. Theor. Phys. **131**, 71 (2020).

[6] R. Ramaswamy, J. M. Lee, K. Cai, and H. Yang, Appl. Phys. Rev. **5**, 031107 (2018).

[7] X. Z. Chen, R. Zarzuela, J. Zhang, C. Song, X. F. Zhou, G. Y. Shi, F. Li, H. A. Zhou, W. J. Jiang, F. Pan, and Y. Tserkovnyak, Phys. Rev. Lett. **120**, 207204 (2018).

[8] J. Železný, H. Gao, K. Výborný, J. Zemen, J. Mašek, A. Manchon, J. Wunderlich, J. Sinova, and T. Jungwirth, Phys. Rev. Lett. **113**, 157201 (2014).

[9] P. Wadley, B. Howells, J. Železný, C. Andrews, V. Hills, R. P. Campion, V. Novák, K. Olejník, F. Maccherozzi, S. S. Dhesi, S. Y. Martin, T. Wagner, J. Wunderlich, F. Freimuth, Y. Mokrousov, J. Kuneš, J. S. Chauhan, M. J. Grzybowski, A. W. Rushforth, K. W. Edmonds *et al.*, Science **351**, 587 (2016).

[10] S. Y. Bodnar, L. Šmejkal, I. Turek, T. Jungwirth, O. Gomonay, J. Sinova, A. A. Sapozhnik, H.-J. Elmers, M. Kläui, and M. Jourdan, Nat. Commun. **9**, 348 (2018).

[11] J. Godinho, H. Reichlová, D. Kriegner, V. Novák, K. Olejník, Z. Kašpar, Z. Šobáň, P. Wadley, R. P. Campion, R. M. Otxoa, P. E. Roy, J. Železný, T. Jungwirth, and J. Wunderlich, Nat. Commun. **9**, 4686 (2018).

[12] P. de V. du Plessis, S. J. van Tonder, and L. Alberts, J. Phys. C **4**, 2565 (1971).

[13] K. Nakahigashi, N. Fukuoka, and Y. Shimomura, J. Phys. Soc. Jpn. **38**, 1634 (1975).

[14] M. Doerr, M. Rotter, and A. Lindbaum, Adv. Phys. **54**, 1 (2005).

[15] A. He, T. Ma, J. Zhang, W. Luo, and M. Yan, J. Magn. Magn. Mater. **321**, 3778 (2009).

[16] R. O. Cherifi, V. Ivanovskaya, L. C. Phillips, A. Zobelli, I. C. Infante, E. Jacquet, V. Garcia, S. Fusil, P. R. Briddon, N. Guiblin, A. Mougin, A. A. Ünal, F. Kronast, S. Valencia, B. Dkhil, A. Barthélémy, and M. Bibes, Nat. Mater. **13**, 345 (2014).

[17] L. C. Phillips, R. O. Cherifi, V. Ivanovskaya, A. Zobelli, I. C. Infante, E. Jacquet, N. Guiblin, A. A. Ünal, F. Kronast, B. Dkhil, A. Barthélémy, M. Bibes, and S. Valencia, Sci. Rep. **5**, 10026 (2015).

[18] Y.-J. Zhang, J.-H. Chen, L.-L. Li, J. Ma, C.-W. Nan, and Y.-H. Lin, Phys. Rev. B **95**, 174420 (2017).

[19] A. A. Sapozhnik, R. Abrudan, Y. Skourski, M. Jourdan, H. Zabel, M. Kläui, and H.-J. Elmers, Phys. Status Solidi Rapid Res. Lett. **11**, 1600438 (2017).

[20] D. Boldrin, A. P. Mihai, B. Zou, J. Zemen, R. Thompson, E. Ware, B. V. Neamtu, L. Ghivelder, B. Esser, D. W. McComb, P. Petrov, and L. F. Cohen, ACS Appl. Mater. Interfaces **10**, 18863 (2018).

[21] P. Sheng, Y. Xie, Y. Bai, B. Wang, L. Zhang, X. Wen, H. Yang, X. Chen, X. Li, and R.-W. Li, Appl. Phys. Lett. **115**, 242403 (2019).

[22] X. Chen, X. Zhou, R. Cheng, C. Song, J. Zhang, Y. Wu, Y. Ba, H. Li, Y. Sun, Y. You, Y. Zhao, and F. Pan, Nat. Mater. **18**, 931 (2019).

[23] H. Yan, Z. Feng, S. Shang, X. Wang, Z. Hu, J. Wang, Z. Zhu, H. Wang, Z. Chen, H. Hua, W. Lu, J. Wang, P. Qin, H. Guo, X. Zhou, Z. Leng, Z. Liu, C. Jiang, M. Coey, and Z. Liu, Nat. Nanotechnol. **14**, 131 (2019).

[24] P. Shirazi, M. K. Panduranga, T. Lee, A. Barra, V. Estrada, D. L. Tran, A. E. Sepulveda, and G. P. Carman, Appl. Phys. Lett. **120**, 202405 (2022).

[25] P. Stremoukhov, C. Davies, A. Safin, S. Nikitov, and A. Kirilyuk, New J. Phys. **24**, 023009 (2022).

[26] Z. Liu, Z. Feng, H. Yan, X. Wang, X. Zhou, P. Qin, H. Guo, R. Yu, and C. Jiang, Adv. Electron. Mater. **5**, 1900176 (2019).

[27] S. V. Peletminskii, Sov. Phys. JETP **10**, 321 (1960).

[28] T. Yamada, J. Phys. Soc. Jpn. **21**, 664 (1966).

[29] E. A. Turov and V. G. Shavrov, Sov. Phys. Usp. **26**, 593 (1983).

[30] V. G. Bar'yakhtar, I. M. Vitebskii, and D. A. Yablonskii, Sov. Phys. JETP **62**, 108 (1985).

[31] M. A. Shamsutdinov, A. T. Kharisov, and A. P. Tankeev, Phys. Solid State **42**, 308 (2000).

[32] Y. V. Gulyaev, S. V. Tarasenko, and V. G. Shavrov, Phys.-Usp. **54**, 573 (2011).

[33] T. V. Bogdanova, D. V. Kalyabin, A. R. Safin, and S. A. Nikitov, J. Phys. D **56**, 205301 (2023).

[34] H. T. Simensen, R. E. Troncoso, A. Kamra, and A. Brataas, Phys. Rev. B **99**, 064421 (2019).

[35] A. B. Shick, S. Khmelevskyi, O. N. Mryasov, J. Wunderlich, and T. Jungwirth, Phys. Rev. B **81**, 212409 (2010).

[36] I. J. Park, T. Lee, P. Das, B. Debnath, G. P. Carman, and R. K. Lake, Appl. Phys. Lett. **114**, 142403 (2019).

[37] A. Barra, J. Domann, K. W. Kim, and G. Carman, Phys. Rev. Appl. **9**, 034017 (2018).

[38] S. Zhuang and J.-M. Hu, npj Comput. Mater. **8**, 167 (2022).

[39] A. V. Azovtsev and N. A. Pertsev, Appl. Phys. Lett. **111**, 222403 (2017).

[40] A. V. Azovtsev and N. A. Pertsev, Phys. Rev. B **100**, 224405 (2019).

[41] A. V. Azovtsev and N. A. Pertsev, Phys. Rev. Mater. **4**, 064418 (2020).

[42] Y. Li, A.-L. Barra, S. Auffret, U. Ebels, and W. E. Bailey, Phys. Rev. B **92**, 140413(R) (2015).

[43] K. Neeraj, N. Awari, S. Kovalev, D. Polley, N. Zhou Hagström, S. S. P. K. Arekapudi, A. Semisalova, K. Lenz, B. Green, J.-C. Deinert, I. Ilyakov, M. Chen, M. Bawatna, V. Scalera, M. d'Aquino, C. Serpico, O. Hellwig, J.-E. Wegrowe, M. Gensch, and S. Bonetti, Nat. Phys. **17**, 245 (2021).

[44] V. Unikandanunni, R. Medapalli, M. Asa, E. Albisetti, D. Petti, R. Bertacco, E. E. Fullerton, and S. Bonetti, Phys. Rev. Lett. **129**, 237201 (2022).

[45] R. Mondal, S. Großenbach, L. Rózsa, and U. Nowak, Phys. Rev. B **103**, 104404 (2021).

[46] L. Winter, S. Großenbach, U. Nowak, and L. Rózsa, Phys. Rev. B **106**, 214403 (2022).

[47] T. Yamada, S. Saito, and Y. Shimomura, J. Phys. Soc. Jpn. **21**, 672 (1966).

[48] A. I. Akhiezer, V. G. Bar'iakhtar, and S. V. Peletminskii, Sov. Phys. JETP **8**, 157 (1959).

[49] C. Kittel, Phys. Rev. **110**, 836 (1958).

[50] M.-C. Ciornei, J. M. Rubí, and J.-E. Wegrowe, Phys. Rev. B **83**, 020410(R) (2011).

[51] F. Keffer and W. O'Sullivan, Phys. Rev. **108**, 637 (1957).

[52] J. Milano, L. B. Steren, and M. Grimsditch, Phys. Rev. Lett. **93**, 077601 (2004).

[53] A. V. Azovtsev and N. A. Pertsev, Phys. Rev. B **94**, 184401 (2016).

[54] M. T. Hutchings and E. J. Samuelsen, Phys. Rev. B **6**, 3447 (1972).

[55] P. de V. du Plessis, S. J. van Tonder, and L. Alberts, J. Phys. C **4**, 1983 (1971).

[56] S. M. Rezende, A. Azevedo, and R. L. Rodríguez-Suárez, J. Appl. Phys. **126**, 151101 (2019).

[57] J. M. D. Coey, *Magnetism and Magnetic Materials* (Cambridge University Press, New York, 2009).

[58] T. Moriyama, K. Hayashi, K. Yamada, M. Shima, Y. Ohya, and T. Ono, Phys. Rev. Mater. **3**, 051402(R) (2019).

[59] We use the measured values of spontaneous strains obtained in Ref. [47], because the values reported in Ref. [13] give enormously high magnetoelastic constants $B_1 = 1.8 \times 10^9$ erg cm^{-1} and $B_2 = 1.05 \times 10^9$ erg cm^{-1} not compatible with other experimental data considered in this paper.

[60] C. Schmitt, L. Baldrati, L. Sanchez-Tejerina, F. Schreiber, A. Ross, M. Filianina, S. Ding, F. Fuhrmann, R. Ramos, F. Maccherozzi, D. Backes, M.-A. Mawass, F. Kronast, S. Valencia, E. Saitoh, G. Finocchio, and M. Kläui, Phys. Rev. Appl. **15**, 034047 (2021).

[61] H. Kondoh, J. Phys. Soc. Jpn. **15**, 1970 (1960).

[62] A. J. Sievers and M. Tinkham, Phys. Rev. **129**, 1566 (1963).

[63] H.-Y. Hao and H. J. Maris, Phys. Rev. Lett. **84**, 5556 (2000).

[64] E. Rongione, O. Gueckstock, M. Mattern, O. Gomonay, H. Meer, C. Schmitt, R. Ramos, T. Kikkawa, M. Mičica, E. Saitoh, J. Sinova, H. Jaffrès, J. Mangeney, S. T. B. Goennenwein, S. Geprägs, T. Kampfrath, M. Kläui, M. Bargheer, T. S. Seifert, S. Dhillon *et al.*, Nat. Commun. **14**, 1818 (2023).

[65] A. V. Azovtsev and N. A. Pertsev, Phys. Rev. B **107**, 054418 (2023).

[66] J. R. Hortensius, D. Afanasiev, M. Matthiesen, R. Leenders, R. Citro, A. V. Kimel, R. V. Mikhaylovskiy, B. A. Ivanov, and A. D. Caviglia, Nat. Phys. **17**, 1001 (2021).

[67] M. Fähnle, D. Steiauf, and C. Illg, Phys. Rev. B **84**, 172403 (2011).

[68] https://rscf.ru/project/23-12-00251/